Acoustical Measurement of Nonlinear Internal Waves Using the Inverted Echo Sounder

QIANG LI AND DAVID M. FARMER

Graduate School of Oceanography, University of Rhode Island, Narragansett, Rhode Island

TIMOTHY F. DUDA

Woods Hole Oceanographic Institution, Woods Hole, Massachusetts

STEVE RAMP

Graduate School of Engineering and Applied Sciences, Naval Postgraduate School, Monterey, California

(Manuscript received 3 July 2008, in final form 5 May 2009)

ABSTRACT

The performance of pressure sensor–equipped inverted echo sounders for monitoring nonlinear internal waves is examined. The inverted echo sounder measures the round-trip acoustic travel time from the sea floor to the sea surface and thus acquires vertically integrated information on the thermal structure, from which the first baroclinic mode of thermocline motion may be inferred. This application of the technology differs from previous uses in that the wave period (~30 min) is short, requiring a more rapid transmission rate and a different approach to the analysis. Sources of error affecting instrument performance include tidal effects, barotropic adjustment to internal waves, ambient acoustic noise, and sea surface roughness. The latter two effects are explored with a simulation that includes surface wave reconstruction, acoustic scattering based on the Kirchhoff approximation, wind-generated noise, sound propagation, and the instrument's signal processing circuitry. Bias is introduced as a function of wind speed, but the simulation provides a basis for bias correction.

The assumption that the waves do not significantly affect the mean stratification allows for a focus on the dynamic response. Model calculations are compared with observations in the South China Sea by using nearby temperature measurements to provide a test of instrument performance. After applying corrections for ambient noise and surface roughness effects, the inverted echo sounder exhibits an RMS variability of approximately 4 m in the estimated depth of the eigenfunction maximum in the wind speed range $0 \leq U_{10} \leq 10$ m s^{-1}. This uncertainty may be compared with isopycnal excursions for nonlinear internal waves of 100 m, showing that the observational approach is effective for measurements of nonlinear internal waves in this environment.

1. Introduction

Nonlinear internal waves (NLIWs) are widely observed in the ocean, especially in coastal waters (Apel et al. 2007; Jackson 2007). Among other properties that have attracted attention over the years is their characteristic shape, which is often associated with a balance between nonlinearity and dispersion, allowing NLIWs to propagate great distances with nearly constant characteristics. Recent interest in these waves is motivated by their roles in energy dissipation and mixing, coastal biological activities, sediment resuspension, offshore engineering, and underwater acoustics (Duda and Farmer 1998; Apel et al. 2007). The physics of generation and propagation have been reviewed by several authors (Apel et al. 2007; Helfrich and Melville 2006), although many aspects remain poorly understood, motivating development of improved observational techniques. The pressure sensor–equipped inverted echo sounder (PIES) is a relatively inexpensive and easily deployed instrument that has the potential for effective measurement of nonlinear internal waves. The concept of inverted echo

Corresponding author address: David M. Farmer, 215 S. Ferry Rd., Narragansett, RI 02882.
E-mail: dfarmer@gso.uri.edu

DOI: 10.1175/2009JTECHO652.1

© 2009 American Meteorological Society

sounders was first developed by Rossby (1969), who showed that the vertical round-trip travel time of an acoustic pulse allowed measurement of the variation of thermal stratification caused by internal tides. They have been deployed in many areas to study such diverse oceanic phenomena as planetary waves, mesoscale eddies, and large-scale circulation (Watts et al. 2001). Here, we explore the performance of the instrument, especially for the study of nonlinear internal waves, using a combination of direct comparisons and model analysis to reveal the potential and limitations of this measurement approach.

The acoustic travel time τ measured by the inverted echo sounder is related to the sound speed profile:

$$\tau = 2 \times \int_{-H}^{\bar{\xi}} \frac{dz}{c(z)} + \varepsilon = 2 \times \int_{-H}^{0} \frac{dz}{c(z)} + 2\frac{\bar{\xi}}{c(0)} + \varepsilon, \qquad (1)$$

where $c(z)$ is the vertical sound speed profile, $\bar{\xi}$ represents the sea surface elevation caused by low-frequency barotropic motion such as the tides, H is the instrument depth, and ε represents fluctuations in measured travel times resulting from variability in scattering of the acoustic signal by a rough sea surface and effects resulting from ambient noise. The geometry is sketched in Fig. 1. The primary factor affecting travel time is the sound speed profile $c(z)$, which changes over short periods (minutes to hours) because of internal tides or passage of nonlinear internal waves. Barotropic effects, such as tides, atmospheric pressure, and the local hydrostatic adjustment associated with baroclinic motions, affect the mean surface elevation $\bar{\xi}$.

We modified pressure sensor–equipped inverted echo sounders in order to transmit at a repetition rate of 6 s, and we deployed the instruments in the South China Sea to observe nonlinear internal waves. Two of these instruments were deployed in a pilot study in 2005 and the other three were deployed in 2007, with locations close to 21°N (see Fig. 2a and Table 1) in the South China Sea. The seasonal variability in the South China Sea is not great and temperature/salinity (T/S) profiles acquired at deployment and recovery in each case are also shown in Fig. 2b. The sound speed profile is calculated from the averaged temperature and salinity data.

The inverted echo sounder measures changes in the vertically integrated sound speed, which depend on the temperature. The strong interaction between the tidal current and Luzon Strait topography launches internal waves westward into the South China Sea. The maximum amplitude of the internal waves can reach 150 m. Defining the scale of waves as the separation of half amplitude points, their wavelength is ~5 km and their period is ~30 min; they propagate westward across the deep basin as extended arcs of up to 200-km length at a speed of ~3 m s^{-1}. The new instruments sampled acoustic travel time every 6 s and bottom pressure every 12 s.

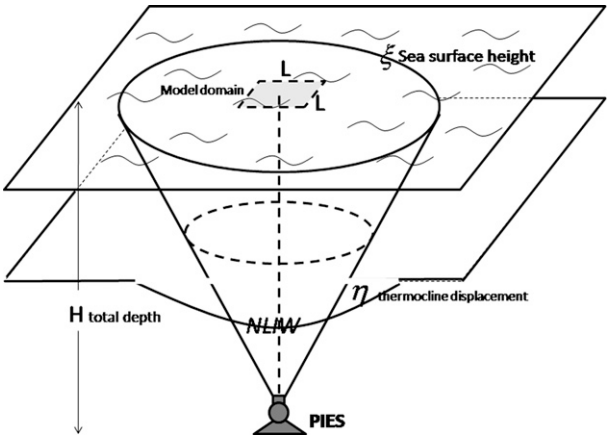

FIG. 1. Sketch of PIES deployment. The round-trip acoustic travel time varies with changes in stratification (represented here by a thermocline displacement η). Only a small portion of the rough surface ξ contributes to the acoustic travel time; it is enclosed within the square $L \times L$ in our model simulation.

Following a brief discussion of measurement principles (section 2), we identify sources of bias and error (section 3) and analyze the contribution of sea state and ambient noise to scatter of the data (sections 4 and 5). This paper concludes with direct comparisons of observations with independent thermistor chain measurements using a fully nonlinear model (section 6). The data analysis procedures, including bias correction, will have applications to measurements taken in other environments and for other purposes.

2. Measurement principles

The goal of our measurements is to obtain acoustic travel time variability, from which we can derive internal wave properties. Before analyzing the technical performance of the instrument, we provide a brief example of the data acquired along with a preliminary analysis.

Displacement of the thermocline is caused by many oceanic dynamical processes, including internal waves and geostrophic eddies. Over the time scales of interest here, the dominant source of variability is internal waves. At a given pressure, the speed of sound is greater in warm water than in cold water. A deepening of the thermal stratification thus decreases the return acoustic travel time. For specific hydrographic conditions, the relationship between displacement of the thermocline and acoustic travel time can be calculated based on normal mode theory, although for nonlinear waves the

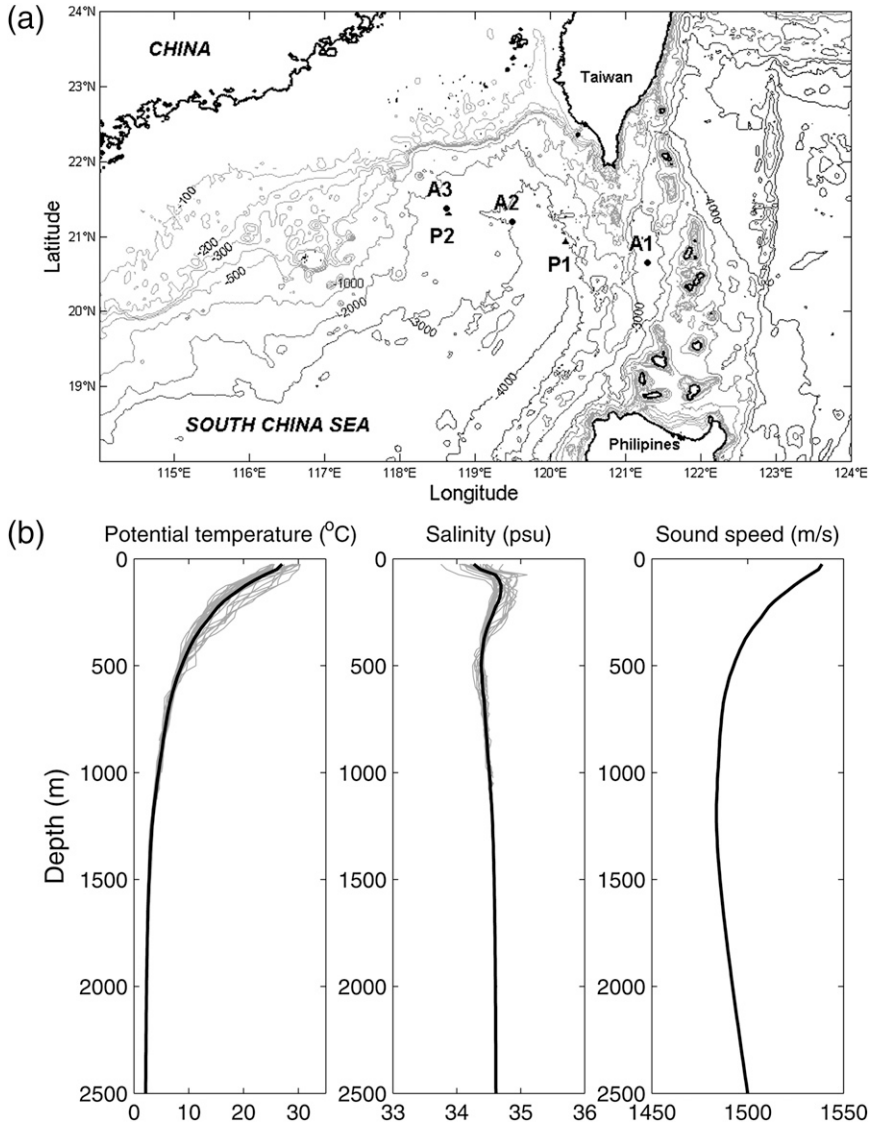

FIG. 2. (a) Topography of the South China Sea and locations of inverted echo sounders deployed in 2005 (P1 and P2) and 2007 (A1, A2, and A3). (b) Potential T/S profiles (gray) with mean profiles (black) superimposed. (right) Mean sound speed profile.

appropriate nonlinear theory will be required. Figure 3a shows eigenfunctions for representative stratification in the South China Sea, which was calculated using both linear (three modes) and also a nonlinear theory, which will be discussed subsequently. The resulting density profile calculated from Fig. 2b leads to an eigenfunction maximum of the first normal mode at ~700 m. Thus, models of the eigenfunction lead to a relationship between wave amplitude and travel time. For any given eigenfunction response, the corresponding temperature

TABLE 1. Deployment locations and times, South China Sea in 2005 and 2007.

Station	Lat	Lon	Deployment date	Recovery date	Depth (m)
P1	21°21.797N	118°35.240E	1643 UTC 26 Jul 2005	3 Nov 2005	2514
P2	20°55.841N	120°12.517E	0431 UTC 25 Jul 2005	3 Nov 2005	3334
A1	20°39.000N	121°17.995E	1604 UTC 5 Apr 2007	2010 UTC 11 Jul 2007	3671
A2	21°12.000N	119°30.000E	0956 UTC 6 Apr 2007	1952 UTC 10 Jul 2007	3160
A3	21°22.302N	118°37.107E	0605 UTC 7 Apr 2007	0048 UTC 10 Jul 2007	2476

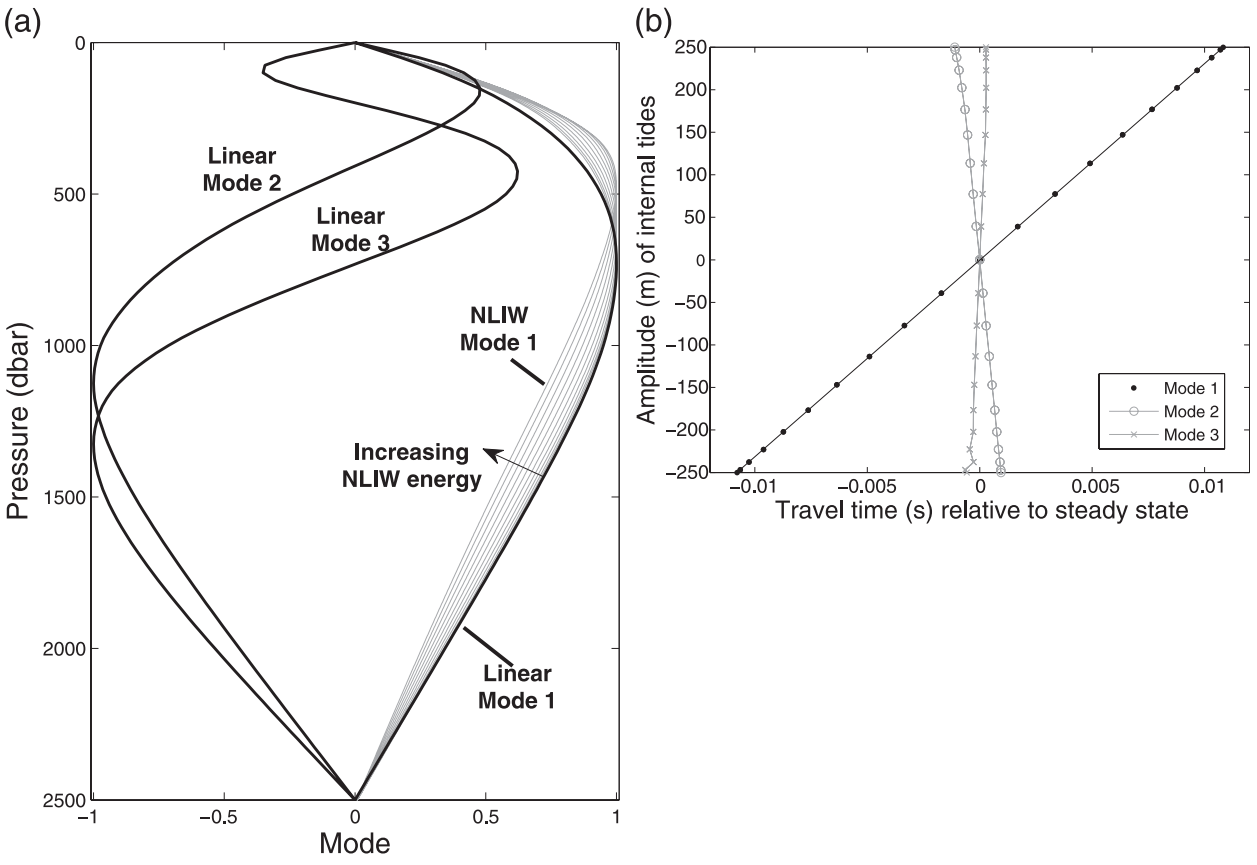

FIG. 3. (a) First 3 normal modes from the linear theory (black) and first mode for the DJL model (gray). The total water depth is assumed to be 2500 m. The arrow superimposed on the DJL internal wave modes indicates the change in shape with increasing wave energy. (b) Relationship between acoustic travel time and internal wave amplitude according to the normal mode analysis shown in (a). The linear regression for mode 1 satisfies the straight line equation $y = (24.1x - 0.0003) \times 10^3$, where y is the amplitude of the internal wave in meters and x is the deviation in acoustic travel time from the mean in seconds. Note that this is calculated for a water depth of 2500 m and the nominal stratification shown in Fig. 2b.

and salinity change may be evaluated: hence, the result in sound speed profile. Integration of this profile leads to the corresponding travel time. The relationship between the first mode eigenfunction maximum and acoustic round-trip travel time is shown in Fig. 3b. It is linear with a sensitivity of 1-ms travel time change corresponding to a 24-m thermocline fluctuation. However, the travel time is essentially insensitive to baroclinic motions of mode 2 and higher. Acoustic travel time measurement is therefore especially appropriate for first mode motions such as the internal waves of interest here.

3. Sources of bias and error in inverted echo sounder measurements

a. Effects of barotropic tides

Barotropic tides elevate or depress the sea surface, increasing or decreasing the total depth of the water column, which results in an increase or decrease in acoustic travel time, respectivly. If the sound speed is 1500 m s^{-1}, then a 1-m surface tide will cause a change in round-trip travel time of 1.3×10^{-3} s. For our observation in the South China Sea, a millisecond travel time change is equivalent to a 24-m isopycnal displacement at the eigenfunction maximum, yielding a 32-m error in the thermocline displacement estimation for a 1-m surface tide. This error is easily corrected by using the measured pressure signal. The bottom pressure includes both hydrostatic and nonhydrostatic components from internal waves. These effects, which have been discussed for shallow (124 m) measurements of nonlinear internal waves (Moum and Smyth 2006), are also detectable for the nonlinear internal waves described here. Our measurements show a pressure decrease of ~0.04 dbar associated with a nonlinear internal wave of amplitude ~100 m. Although these signals are of some interest in their own right, they are quite small and subject to contamination by barotropic signals.

b. Hydrostatic effects from baroclinic motion (internal tides)

As the thermocline deepens during passage of an internal wave, the sea surface is elevated to balance the deceleration. A simple illustration for nonlinear internal waves is provided by calculating the thermocline displacement η for a wave by using the two-layer Korteweg–de Vries (KdV) solution:

$$\eta(x, t) = \eta_0 \operatorname{sech}^2 \frac{x - Vt}{\Delta}. \tag{2}$$

The nonlinear velocity V and characteristic width Δ are related to the linear wave speed c_0 and the amplitude of the wave η_0:

$$V = c_0 + \frac{\alpha\eta_0}{3} \quad \text{and} \quad \Delta^2 = \frac{12\beta}{\alpha\eta_0}, \tag{3}$$

where α and β are the nonlinear and dispersion parameters, respectively, that are determined by the local stratification. The velocity in the upper layer can be obtained from the continuity equation with the steady wave assumption ($X = x - Vt$):

$$u_1 = -\frac{V}{h_1}\eta. \tag{4}$$

The surface elevation is then obtained by integrating the horizontal momentum equation assuming η vanishes at $x \to \pm\infty$:

$$\begin{aligned} \xi &= -\frac{1}{g}\int_{-\infty}^{x} \frac{Du_1}{Dt}\, dx' = -\frac{1}{g}\int_{-\infty}^{\xi} (u_1 - V)\frac{du_1}{dx'}\, dx', \\ &= -\frac{V^2}{gh_1}\left(\frac{1}{2}\frac{\eta}{h_1} + 1\right)\eta \approx -\frac{V^2}{gh_1}\eta. \end{aligned} \tag{5}$$

Thus, the ratio between the surface elevation and interface depression is $\sim(V^2/gh_1)$, which is primarily determined by the local stratification. This result reduces to the linear solution $\xi/\eta = \Delta\rho/\rho_0 \times h_2/(h_1 + h_2)$ if $V = [\Delta\rho/\rho_0 \times gh_1h_2/(h_1 + h_2)]^{1/2}$ for $\eta \ll h_1$, where h_1 and h_2 are upper- and lower-layer thicknesses in a two-layer fluid, $\Delta\rho$ is the density difference, and ρ_0 is the mean density. In the South China Sea, the sea surface elevation is about 0.18 m for a 100-m thermocline depression corresponding to a 0.24×10^{-3} s increase in travel time. This is equivalent to the effect of a 6-m isopycnal displacement at the eigenfunction maximum. This modest (~4%) correction is readily included in calculations of internal wave properties derived from inverted echo sounder measurements.

c. Effect of sea state and ambient noise

Additional effects resulting from sea state and ambient noise are represented by the term ε in Eq. (1). From the measured temperature profiles at station P2, we found that, in the absence of internal wave packets, the background internal wave field with period less than 30 min contributes an RMS variability in isotherm displacement maxima of ~3 m. With rising wind speed, the measurement is simultaneously influenced by the increase in surface roughness and the increase in wind-generated ambient noise. The joint consequence of these effects is the primary reason for the scattered distribution of travel times apparent in Fig. 4. In this section, we seek to explain this variability. Ambient noise is a passive variable in this process, which is mainly determined by wind speed in the frequency band 1–25 kHz (Knudsen et al. 1948). Acoustic scattering from a rough surface has been well studied by the acoustic and remote sensing community. The scattering is determined by the properties of the acoustic system and by the characteristics of the rough sea surface. (We note here that effects resulting from advection or refraction of the acoustic pulse by the current are small. Vertical advection effects are negligible for the two-way propagation; horizontal shear effects are governed by the Mach number $M \sim 1/1500$, and they are also negligible.)

Lord Rayleigh studied the scattering of sound waves at a sinusoidal boundary (Rayleigh 1877; Beckmann and Spizzichino 1963; Fortuin 1970). Holford (1981) proposed an exact solution of the scattering of sound for a sinusoidal pressure-release surface, although numerical implementation is difficult. Having solved the problem for a periodic surface, the result is readily extended to an arbitrary random surface via Fourier superposition (Rice 1951). Eckart (1953) calculated the Helmholtz integral by applying two boundary conditions: one is the pressure-release surface and the other is obtained from the method of physical optics (i.e., the Kirchhoff approximation, which requires that the normal derivative for the incident and reflected waves be equal). Clay (1960) compared these theories with experimental results from Brown and Ricard (1960).

Rayleigh's method requires the surface slope be sufficiently small. The Kirchhoff approximation is valid under the restriction that the radius of curvature R_c obeys the inequality

$$R_c \geq \frac{\lambda}{\pi \sin^3\theta}, \tag{6}$$

where θ is the local grazing angle (i.e., the angle with respect to the horizon) and λ is the wavelength of the incident waves. To avoid the above restrictions, a composite-roughness theory was developed (Kur'ynov

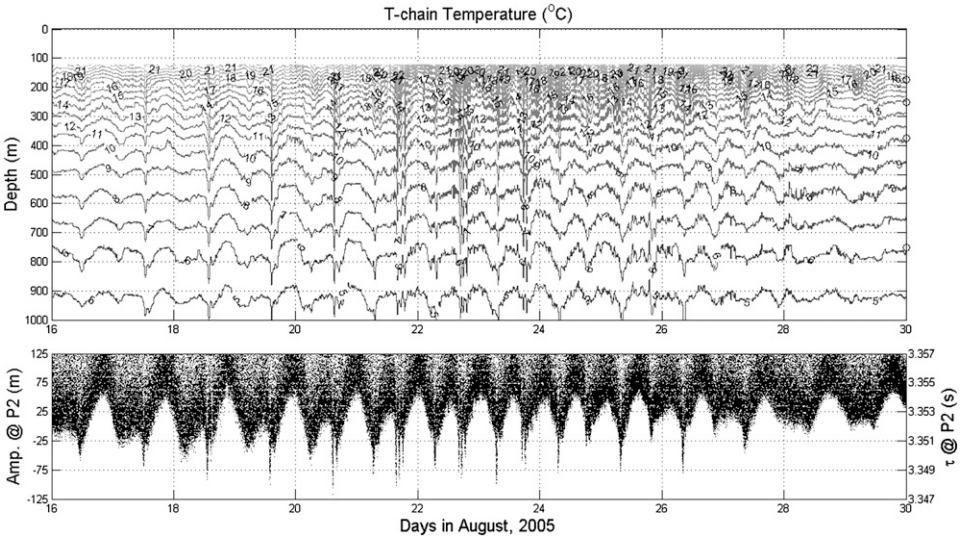

FIG. 4. (top) Temperature contours at station P2 derived from a thermistor chain mooring located 6 km west of P2 (Fig. 2a). The contour interval is 1°C. (bottom) Raw acoustic travel times derived from the inverted echo sounder at P2.

1963; McDaniel and Gorman 1983), in which the sea surface is split into two components: a large-scale and a small-scale surface, which correspond to the Kirchhoff and Rayleigh approximations, respectively. McDaniel (1986) improved this method to reduce dependence on the scale separation criteria and also showed that, for large grazing angles (>70°), the contribution of the large-scale surface is dominant. Therefore, for the present implementation, the Kirchhoff approximation is appropriate.

Scattering from resonant subsurface bubbles is another potential source of surface reverberation. The bubble radius at resonance a_r for a 12-kHz acoustic signal of $f = 12$ kHz is $a_r = 3.2f^{-1} = 267$ μm. The scattering contribution is determined by bubble density and distribution, which is also related to the surface wind. For the acoustic frequency range 3–25 kHz, backscattering at grazing angles above 30° is found to be in agreement with the predictions of rough surface scattering theory (McDaniel 1993). Very high attenuation by bubbles can occur sporadically near the surface at high wind speeds (>10 m s^{-1}). Bubbles can also affect ambient noise. Farmer and Lemon (1984) showed that at higher frequencies the ocean becomes a quieter place as the wind increases above about 10 m s^{-1}, because the sound generated by breaking waves is attenuated by bubble clouds. The effect is modest at 8 kHz but significant at 14.5 kHz, which suggests that our 12-kHz signals will be affected above 10 m s^{-1}. At still higher acoustic frequencies (~100 kHz), bubble densities may occasionally become so great that they mask the surface from active sonar systems (Farmer et al. 2002) and show up as increased noise in travel time measurement; however, at 12 kHz and for wind speeds representative of most of our data, the primary effect of bubbles is likely to be to reduce ambient noise in the upper wind speed range. Bubbles also change the effective sound speed. However, this is only significant very close to the sea surface, and it is also intermittent. Taking Terrill and Melville's (1997) results as a guide, the effective sound speed correction of the surface bubble layer at a wind speed of 10 m s^{-1} will be a maximum, although sporadic, increase in acoustic travel time of 0.1 ms. This corresponds to an increase of the depth of the eigenfunction maximum of 2.4 m.

4. Contribution from the sea state

a. Numerical simulation of the transducer

The pressure-equipped inverted echo sounder is composed of an anchor stand, acoustic release, internal circuit, and a transducer (ITC-3431C). In the South China Sea experiment, the instrument was set to transmit an acoustic pulse with a 6×10^{-3} s duration. The carrier frequency of the acoustic pulse is $f_c = 12$ kHz. For a nominal sound speed of 1500 m s^{-1} at the source, the carrier acoustic wavelength is $\lambda = 0.125$ m. The shape of the transducer is a circular piston with radius $a = 5$ cm. In the far field, the acoustic signal can be computed in cylindrical coordinates (r, θ) by the integration of point sources:

$$p(r, \theta, t) = \frac{j}{2} A_1 \frac{a}{r} ka \left[\frac{2J_1(ka \sin\theta)}{ka \sin\theta} \right] e^{j(2\pi f_c t - kr)}, \quad (7)$$

where J_1 is the first-order Bessel function of the first kind, k is the wavenumber, and A_1 is a constant related to the transducer power.

The transducer directs a pulse of duration $T_0 = 6$ ms upward. Given a rectangular pulse

$$p_0 = A(r, \theta) \times \text{rect}\left(\frac{t}{T_0}\right) e^{j2\pi f_c t}, \quad (8)$$

the corresponding frequency representation is

$$P(f) = A(r, \theta) T_0 \,\text{sinc}[(f - f_c) T_0], \quad (9)$$

where the amplitude $A(r, \theta)$ is determined by the transducer properties [i.e., Eq. (7)].

b. Numerical simulation of the sea surface

Acoustic scattering at the rough sea surface is determined by the characteristics of the interface. The sea surface elevation ξ is defined as the vertical displacement from the mean water level of the ocean surface or

$$\langle \xi^2 \rangle = \int_0^\infty S(\omega)\, d\omega, \quad (10)$$

where $S(\omega)$ is the surface wave spectrum. The Pierson–Moskowitz (PM) spectrum, based on a similarity theory for a fully developed sea state (Pierson and Moskowitz 1964), is

$$S(\omega) = \frac{\alpha_{\text{PM}} g^2}{\omega^5} \exp\left[-\frac{\beta_{\text{PM}} g^4}{(\omega U_{19.5})^4} \right], \quad (11)$$

with parameters $\alpha_{\text{PM}} = 8.10 \times 10^{-3}$, $\beta_{\text{PM}} = 0.74$, and $g = 9.81$ m s^{-2}. The wind speed $U_{19.5}$ is defined at 19.5-m height, which for convenience is converted to an equivalent 10-m height through the empirical relationship (Charnock 1955):

$$U_z = \frac{u_*}{0.4} \ln\left(\frac{z}{z_0}\right) \quad \text{and} \quad (12)$$

$$\frac{z_0 g}{u_*^2} = 0.015. \quad (13)$$

The Pierson–Moskowitz spectrum is a superposition of linear waves, and therefore does not properly represent the peaked shape of individual wave crests. It is also an equilibrium wave spectrum and thus less representative of changing wind conditions. The measurement and modeling of the detailed time evolving shape and structure of the sea surface under changing wind conditions remains an active area of research. Wind-generated surface waves include three dynamical processes: energy input from the wind, wave–wave interactions, and dissipation by wave breaking (Phillips et al. 2001). Theories such as the weak turbulence theory (Kitaigorodskii 1992) and the equilibrium range theory (Phillips 1985) have been proposed to describe the statistical dynamics of surface waves. For large amplitude nonlinear internal waves, strong convergence and divergence of the surface current can also increase or decrease the energy spectral density. In the face of this very complicated environment, we have chosen to represent the waves by the Pierson–Moskowitz equilibrium spectrum with its simple superposition of linear wave components. The general consistency of the results with our observations discussed below suggests that this is a reasonable first approximation. However, more comprehensive and accurate representation of the surface environment and its resulting contribution to surface scatter is certainly justified, especially if further development of the instrument is pursued, allowing it to collect the raw surface scattered signal. In particular, surface roughness modulation by internal waves may be detectable. Although this raises intriguing measurement possibilities, such observations lie beyond the scope of the present study.

We are interested in the spatial structure of the sea surface and thus convert the Pierson–Moskowitz spectrum into the wavenumber domain by using the deep water dispersion relationship

$$\omega^2 = gK. \quad (14)$$

The wavenumber spectrum is then

$$W(K) = S(\sqrt{gK}) \frac{1}{2} \sqrt{\frac{g}{K}} = \frac{\alpha_{\text{PM}}}{2K^3} \exp\left[-\beta_{\text{PM}} \frac{g^2}{U_{19.5}^4 K^2} \right], \quad (15)$$

where $K = \sqrt{k_x^2 + k_y^2}$ is the vector wavenumber. The radial symmetry of the transducer renders the instrument insensitive to directional properties of the surface, so directivity is neglected here (this simplification would not apply if wave–wave interaction was incorporated). Each Fourier component is superposed with random phase. The equilibrium assumption implies that the sea surface is only dependent on the wind speed. Surfaces generated with wind speeds taken from Quick Scatterometer (QuikSCAT) observations are used in the computation, and the results are compared with measured scatter in acoustic travel times.

c. Numerical simulation of acoustic backscattering and propagation

The transducer emits a 12-kHz acoustic pulse from the sea floor ($z = -H$) to the sea surface at $z = 0$. For the purpose of evaluating contributions from ambient noise and surface roughness, we assume a uniform nominal sound speed ($c_{s0} = 1500$ m s^{-1}) in the water column; specifically, we assume that changes in sound speed stratification resulting from internal waves are not directly coupled to the surface scattering problem. When the sound wave arrives at the sea surface, the amplitude and phase of the acoustic field can be obtained analytically, based on the properties of the transducer. Small incident angle scattering satisfies the Kirchhoff approximation. With the pressure-release boundary condition, the sea surface elevation will cause a phase change of the reflected wave equal to

$$\Delta\varphi = 2\pi\frac{2\xi}{\lambda}, \tag{16}$$

with the reflected wave amplitude equal to that of the incident wave. This phase change is incorporated into the subsequent acoustic propagation model as the surface boundary condition.

For computational economy, our calculations were limited to a water depth of $H = 1024$ m. Computation for a depth of 512 m produced essentially the same results. The instrument threshold is adjusted to detect the pulse arrival over an initial time step $\Delta T = 3$ ms. Thus, the total duration of the observed signal is much greater than the short period of useful measurement ΔT and allows us to limit the horizontal range of the calculation domain L accordingly:

$$L > 2\sqrt{2c_{s0}\Delta T H + c_{s0}^2\Delta T^2}. \tag{17}$$

For $H = 1024$ m, $L > 192$ m, the computation domain is chosen to be 200 m $\times$ 200 m. The grid size of 2048 $\times$ 2048 and a vertically integrated step of 4 m are implemented to control aliasing of the surface. Acoustical signals propagating beyond this domain are damped. The transducer is placed in the center of the domain.

Propagation of the acoustic pulse is simulated by using the parabolic equation (PE). Recently, Duda (2006a,b) implemented the PE with a wide-angle split-step algorithm (Thomson and Chapman 1983) to study three-dimensional acoustic propagation. The method relies on two assumptions: 1) local variations in refractive index are small and 2) the effective propagation paths are limited to a narrow aperture. Both requirements are satisfied in the present application. Given a rotationally symmetric acoustic field $\psi = p(r, z)\exp(-j\omega t)$ in cylindrical coordinates (r, θ, z), the pressure resulting from a point source satisfies the Helmholtz equation

$$\frac{1}{r}\frac{\partial}{\partial r}\left(r\frac{\partial p}{\partial r}\right) + \frac{\partial^2 p}{\partial z^2} + k_0^2 n^2 p = 0, \tag{18}$$

where $n(r, z) = c_{s0}/c_s(r, z)$ is the acoustic refractive index, which is determined by the ratio of a reference sound speed c_{s0} to the sound speed c_s of the medium; $k_0 = \omega/c_{s0}$ is the reference wavenumber.

With the transformation

$$p(r, z) = \frac{u(r, z)}{\sqrt{r}} \tag{19}$$

and the adoption of two operators

$$P = \frac{\partial}{\partial r} \quad \text{and} \quad Q = \left(n^2 + k_0^{-2}\frac{\partial^2}{\partial z^2}\right)^{1/2}, \tag{20}$$

(18) can be transformed into parabolic form

$$Pu = ik_0 Qu, \tag{21}$$

which admits numerical solution without iteration. Finite bandwidth pulses are simulated by using Fourier synthesis.

d. Estimation of ambient noise and transmission loss

To minimize instrument energy requirements, the output power of the transducer is set relatively low, sound pressure level being adjusted from 170 to 200 dB re 1 μPa at 1 m from the transducer, depending on deployment depth. Ambient noise is closely related to wind speed in the bandwidth of interest (Knudsen et al. 1948). The ambient noise level at 12 kHz varies from 40 to 60 dB re 1 μPa Hz$^{-1/2}$ through the wind speed range 1–15 m s^{-1} (Wenz 1962). Other unknown noise, including instrument noise, is estimated to be less than 10 dB re 1 μPa Hz$^{-1/2}$ based on a pilot test. Use of a narrowband-limited filter in the PIES circuit justifies representation of the noise by a white Gaussian signal. The energy loss resulting from scattering and transmission spreading is given by the PE model. Transmission loss resulting from absorption is small and ignored (Urick 1983). We calculate a 10–30-dB difference between the maximum received pulse level and the noise level over the wind speed range $1 \le U_{10} \le 15$ m s^{-1}. The attenuation of 12-kHz noise by bubble clouds at wind speeds above 10 m s^{-1} was identified in section 3c, but our data are few and scattered at these wind speeds and this effect is not explicitly included in the simulation.

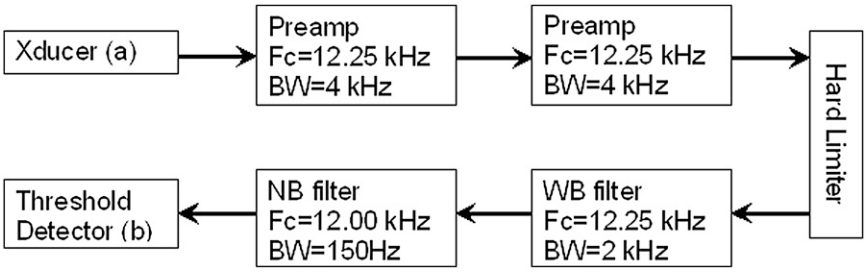

FIG. 5. Flowchart of the simulated analog circuit of the inverted echo sounder detection unit.

e. Numerical simulation of the circuit detection

The circuit design employs a hard limiter and threshold detection technique. Figure 5 shows the circuit's flowchart. Analog Butterworth filters are implemented for the broad- and narrowband filters. The 6-ms CW pulse (Fig. 5, left panel) drives the numerical model of the circuit. Figure 6 shows the comparison between numerical simulation of the circuit and a laboratory measurement. The envelope of the signal is shown as the solid line in the right panel of Fig. 6, and it is generally consistent with the analog test. If the threshold is set to 0.9 V, there will be a 3-ms delay between the pulse arrival time and the time detected by the instruments.

The received signals can be derived from the PE model through inverse Fourier transformation and deconvolution. As expected, the signal is quite variable, depending on the precise phase choice for each component of the surface wavenumber spectrum or the precise detection point on the sea floor. During a test of the instrument, we recorded a short set of raw pulses. As with the modeled pulse, the raw signals were highly variable, limiting the value of direct comparison at this stage of the processing. The deconvolved signal, together with the ambient noise, is used to drive the analog circuit simulation and calculate travel time. For computational efficiency, sample sound pressure values from a random walk on the sea floor are used to avoid repeating lengthy calculations of many transmitted pulses. The resulting simulations can then be compared with observations.

5. Comparison with the observations

The measured acoustic travel time variability during the 2007 experiment in the South China Sea (Fig. 2) became the basis for comparison with our model calculations. During the field observations, the travel times were recorded every 6 s. For the purposes of modeled scattering comparisons, we selected 1 h of data following each QuikSCAT pass. We eliminated the only coincidence of nonlinear internal waves with these data segments and calculated arrival times by using a linear least squares fit to remove trends associated with baroclinic motion, primarily the internal tide. Figure 7 compares the modeled travel time scatter with the observed scatter at wind speeds of 5 and 10 m s^{-1} based on QuikSCAT wind measurements for the instrument locations. The shape of the distribution curves is similar. This comparison is for station A1. The probability distribution is broader at higher wind speeds; there is some variability in width comparisons for different deployment locations, but the overall shape is quite similar, especially at 10 m s^{-1}.

The observed travel time distribution appears to approximate the Rayleigh distribution:

$$y = f(\tau|\tau_0, b) = \frac{\tau - \tau_0}{b^2} \exp\left[-\frac{(\tau - \tau_0)^2}{2b^2}\right], \qquad (22)$$

where the dimensional parameter b defines the width of the distribution, with τ_0 being the point at which the distribution is zero (i.e., the minimum travel time within the period of measurement). This distribution provided a basis for comparison of the model with 3 months of data from three instruments, which are shown in terms of the Rayleigh parameter b as a function of U_{10} in Fig. 8. The Rayleigh distribution is consistent with an echo ensemble composed of members with each having dominant energy arriving from surface locations at radial distances from zenith, which also follows a Rayleigh distribution; this is the distribution of distances from

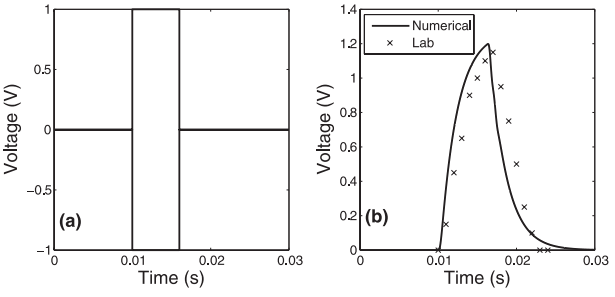

FIG. 6. (a) A CW wave with 6-ms duration is used to drive the numerical simulation of the analog circuit. (b) Comparison between laboratory result and simulation.

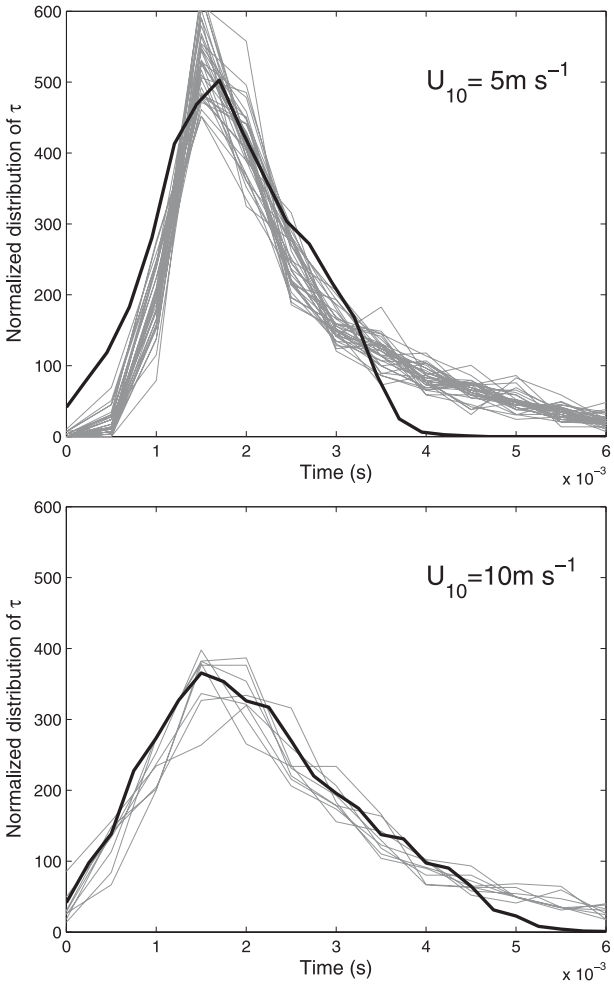

FIG. 7. Comparison between the observations (gray) and model simulation (black) of acoustic travel time distributions at the wind speeds of 5 ± 1 and 10 ± 1 m s^{-1}. The distribution is normalized by the sample length and the bin width. The observed travel times are derived from 1 h of data after the QuikSCAT passes with 0.5-ms bin width.

zenith of an ensemble of positions with latitude and longitude perturbations (from zenith) uncorrelated and each normally distributed. The parameter b corresponds to the standard deviation of the extra distance covered by the dominant sound. To translate from distance to time, note that reflection from a position 56 m from zenith to a PIES at 1024-m depth would have a delay time of 2 ms. Note that the arrival time anomalies caused by increased distance anomalies to wave crests and troughs will add a normally distributed component to the arrival time distribution, which is apparently a small effect.

The model results (solid black squares) are also superimposed on the observations in Fig. 8. The distribution width b, although exhibiting substantial scatter, is approximately linear, which satisfies the relationship

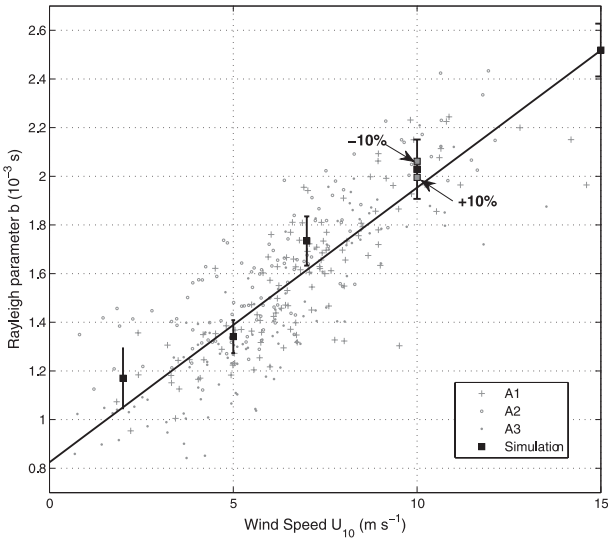

FIG. 8. The Rayleigh distribution (22) is used to fit the observed and modeled travel times. The wind speed is acquired from QuikSCAT. Acoustic travel time data are calculated for 1 h following the satellite pass over the instruments. The Rayleigh parameter b, defining the width of the distribution function, is linearly related to wind speed. Increasing the ambient noise input to the model by $\pm 10\%$ of the Knudsen et al. (1948) prediction changes the Rayleigh width prediction by $\pm 5\%$, which is shown here for $U_{10} = 10$ m s^{-1}.

$$b = 0.11 \times U_{10} + 0.82, \tag{23}$$

where the Rayleigh parameter b is expressed in milliseconds and U_{10} is in meters per second. There is also some stratification of the data, with points for station A2 exhibiting generally larger values of the Rayleigh width b than points for A1. This is likely due to variations in instrument sensitivity, power settings, fetch, and environmental factors. Nevertheless, considering the linear representation of surface waves and the equilibrium wave spectrum assumption, the model performance appears generally consistent and provides support for its application to optimizing instrument setup and evaluating errors and biases.

The numerical simulation can be used to evaluate travel time bias (Fig. 9). This is expressed as a function of wind speed U_{10} and Rayleigh width b, which can be evaluated from the data directly. To the extent that the Rayleigh function is an effective approximation of the travel time scatter, the delay to the arrival of the distribution peak τ_p is directly related to the width b:

$$\tau_p = \tau_0 + b. \tag{24}$$

The distribution width increases with surface roughness, which in turn increases with wind speed. The leading edge of the travel time arrival, which is the zero point τ_0 of the Rayleigh distribution, decreases with wind speed.

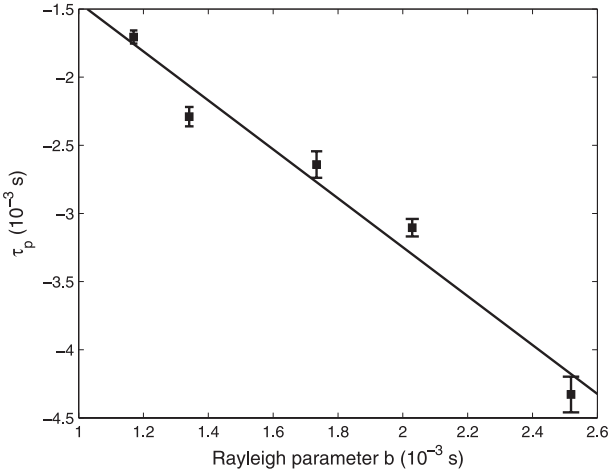

FIG. 9. The bias in acoustic travel times resulting from sea surface roughness and ambient noise can be evaluated from the simulation. The peak value of the distribution function τ_p shifts earlier with increasing wind speed.

This is to be expected because the first arrivals will be reflected from the troughs of the longer waves, the amplitude of which increases with increasing wind speed. On the other hand, an increase in the ambient noise delays detection time because detection must be above the noise level, thus tending to reduce the delay to the distribution peak. This has the effect of decreasing the calculated Rayleigh width b. In this way, the effect of ambient noise works in opposition to the effect of surface roughness. However, the positive slope in Fig. 8 indicates that surface roughness effects dominate. For example, if we take the model calculations at a wind speed of 10 m s^{-1} and run the model with the same surface roughness but with ambient noise increased by 10%, the effect is to decrease the Rayleigh width b by 5%. For a corresponding 10% decrease in ambient noise, the distribution width b is increased by 5%.

The peak value of the Rayleigh distribution, which occurs at $\tau_0 + b$, declines with increasing wind speed. This means that the distribution shifts to an earlier pattern of arrival times with increasing wind speed. This bias can be expressed as

$$\tau_p = -0.20U_{10} - 1.27 = -1.80b + 0.34, \qquad (25)$$

where U_{10} is in meters per second, τ_p is in milliseconds, and b is defined in Eq. (24). For a 10 m s^{-1} wind, this corresponds to a bias of -1.59×10^{-3} s total travel time relative to a 2 m s^{-1} wind, which is equivalent in the South China Sea to a baroclinic displacement of 38 m. The data are very limited and scattered above 15 m s^{-1}, and no useful extrapolation is proposed. It is anticipated that bubble attenuation of ambient noise would have the effect of reducing the Rayleigh width below that predicted with the bubble-free simulation. Subject to this constraint, the model calculations provide a consistent basis for correcting bias.

Based on the above discussion, an optimal data processing method can be proposed to estimate travel times from the scattered data and remove bias caused by sea surface roughness and ambient noise. First, the original data are grouped into specified bins of an appropriate sample length for analyzing bias (~100 points or more). The Rayleigh functional approximation is then fitted to the data in each bin and the bias removed using Eq. (25); calculation of U_{10} from b may be an additional useful variable. From the pressure sensor time series, a tidal correction is made. Depending on the application, additional correction may be made for barotropic adjustment to baroclinic motions. If high-frequency nonlinear internal waves are the subject of analysis, smaller bins may be required to obtain adequate temporal resolution, and these may not support stable Rayleigh function fits. For example, we used 180-s bins in the South China Sea. In this case, an effective approach involved averaging all values within the first 10^{-3} s of the first acoustic arrival. Wind conditions are unlikely to change much during passage of an individual wave, so correction of bias using the Rayleigh fit discussed is not critical, although it should be included for measuring longer period processes.

6. Analysis of nonlinear internal waves

The gravest empirical mode (Watts et al. 2001) is often used to retrieve the vertical temperature structure from travel times. This method calculates the travel times from historical XBT and CTD data in a specific region and then uses a cubic smoothing spline to obtain an empirical relationship between travel time and vertical temperature profiles, which are then used to populate a lookup table. Once the travel time is known, the estimated vertical temperature profile is recovered. Although this is effective for many purposes, a study of internal wave dynamics over short time scales motivates a different approach. It is still necessary to know the nominal density profile. For our South China Sea studies, we used CTD profiles acquired during our cruises (see Fig. 2b) supported in some cases with moored thermistor data. In the absence of such information, historical records of T/S profiles would be required.

Our observations were acquired close to thermistor moorings where the temperature was recorded at 60-s intervals and at 10 depths down to 2433 m. These data provide an opportunity for comparison with our depth-integrated measurements. Deriving the isopycnal or

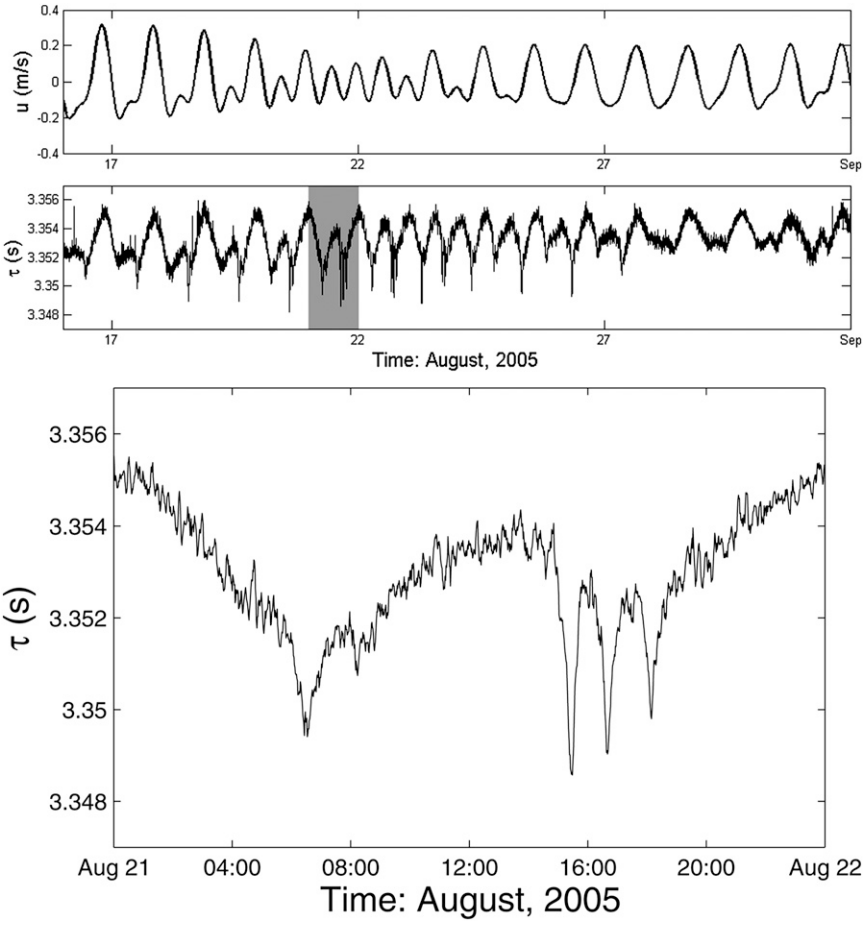

FIG. 10. (top) Zonal tidal current at Luzon Strait (21°N, 122°E). It takes 33 h for waves to propagate from the sill to P2. (middle) Acoustic travel times at P2. (bottom) Enlarged display of acoustic travel times for 21 Aug 2005 used for the NLIW reconstruction in Fig. 11.

isotherm structure of nonlinear internal waves from travel times requires an appropriate model. Here, we illustrate this approach with Long's (1953) fully nonlinear model, which is based on the Dubriel-Jacotin (1932) transformation, also called the DJL model. It is assumed that the lower boundary is a streamline, so there is no flow separation, that the flow is steady, and that the conditions far upstream are known (i.e., the vertical profile of the kinetic energy of the upstreamflow is known). Under the Dubriel-Jacotin transformation, the original Boussinesq equations take the form of the Helmholtz equation (Long 1953; Baines 1995):

$$\nabla^2\delta + \kappa^2\delta = 0, \tag{26}$$

where

$$\kappa^2 = \frac{N^2}{U^2,} \tag{27}$$

and $\delta(x, z)$ represents the vertical displacement of the streamline at (x, z). Also, N and U are the upstream buoyancy frequency and horizontal velocity, respectively. The exact solution can be obtained numerically without restrictions on the degree of nonlinearity or the form of stratification (Turkington et al. 1991). In contrast to linear waves, the eigenfunction maximum (Fig. 3) now depends on amplitude. A corresponding nonlinear eigenvalue or wave speed is obtained for each wave amplitude.

For given background stratification, the shape and speed of nonlinear internal waves are determined by the wave amplitude or potential energy. The nonlinear internal wave packet at 1600 UTC 21 August 2005 (Fig. 10) is chosen for analysis and processed as outlined earlier. This packet contains three single waves of progressively decreasing amplitude. The background density profile is obtained by averaging the temperature profiles derived from the thermistor chain over the half hour prior to arrival of the wave packet; salinity data are derived from CTD data based on the water mass properties (salinity

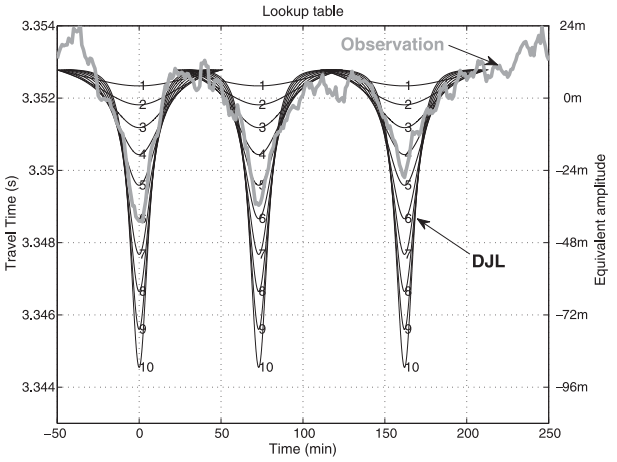

FIG. 11. The acoustic travel times calculated with the DJL model for NLIWs shown in Fig. 10. The calculation is carried out for different energy levels (6, 5, and 4) to identify a best fit.

variability has a very minor effect on the density profile). Thus, a lookup table for the nonlinear internal waves corresponding to a range of different possible energy levels is established. The comparison is shown in Fig. 11.

The observed travel times from the inverted echo sounder (thick gray line in Fig. 11) are superimposed on the DJL prediction for a range of energy levels to find the best fit. The energy levels 6, 5, and 4 are chosen for each wave. The nonlinear eigenfunctions (Fig. 3a) corresponding to each fitted energy level is then used to calculate the modeled isotherm displacement as a function of depth and time. The reconstructed temperatures are compared with the temperatures recorded by the nearby thermistor chain in Fig. 12. The fit is generally consistent with the temperature observations for the first wave but less satisfactory for the second and third. This discrepancy is to be expected, especially with increasing depth as the contributions of neighboring waves combine to increase the isopycnal displacements between successive wave crests. The DJL analysis also gives us the wave speeds (3.20, 3.13, and 3.07 m s^{-1}) that are similar to the estimated wave speeds (3.10 m s^{-1}) based on arrival times at the inverted echo sounder and thermistor chain and the known separation; a similar level of consistency was found for travel times over greater distances based on remote sensing observations. However, it is emphasized that the DJL model is steady state and does not incorporate variability associated, for example, with the internal tide on which the nonlinear waves ride or effects of rotation. A detailed comparison of these data with more comprehensive time-dependent models, free of the assumption of an isolated wave and incorporating rotation, is the subject of a separate analysis.

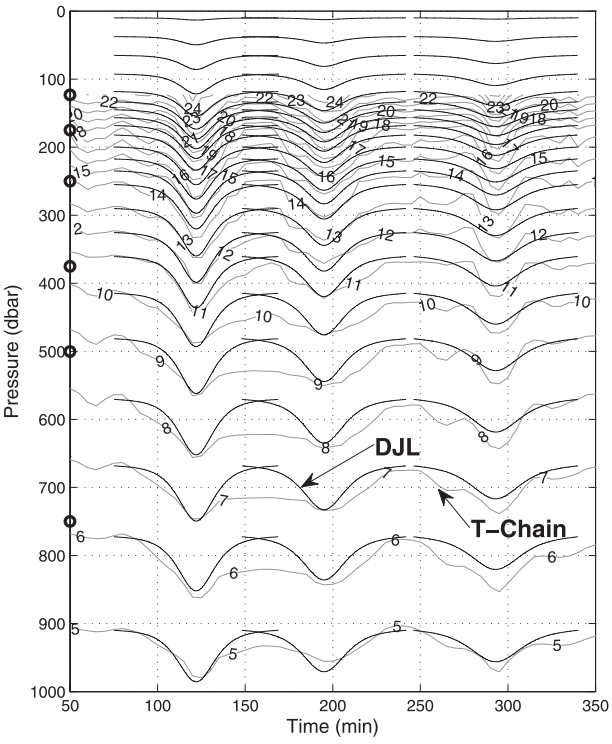

FIG. 12. NLIWs corresponding to Figs. 10 and 11 retrieved directly from acoustic travel times by using the DJL model (black). Simultaneous temperature contours (gray) from thermistor chain data are compared with the DJL predicted isotherm displacements for the upper 1000 m.

7. Summary and discussion

We have shown that the inverted echo sounder can be an effective instrument for measuring nonlinear internal waves in the open ocean. Sources of error affecting instrument performance are analyzed. The error caused by elevation of the sea surface, including barotropic tides and the barotropic pressure adjustment associated with baroclinic motion, can be easily corrected. The acoustic behavior due to the sea state, specifically the combined effect of sea surface roughness and ambient noise, turns out to be a dominant and complicated error source in travel time detection. It introduces variability in the acoustic signal including its detection by the instrument's analog circuit. The effect of sea state has been numerically simulated with a model that includes sea surface reconstruction, acoustic scattering and propagation, ambient noise, and the instrument's electronic detection circuit. The spreading of the travel time reveals an asymmetric pattern approximating the Rayleigh function. The Rayleigh parameter b, defining the width of the travel time probability distribution, increases with increasing wind speed, equivalent to the sound arriving from points within a surface patch of increasing size. The

degrees of sea surface roughness and ambient noise are both monotonically related to the wind speed, and the behavior of travel time distributions are modeled by using an equilibrium wave spectrum and standard ambient noise predictions. Ambient noise tends to oppose the spreading of the distribution by raising the detection threshold, but the effect of ambient noise on the travel time distribution is about half that of the rough surface scattering. Modeled distributions are consistent with the observations, providing a basis for modeling and correcting sea-state bias in measurements.

Given the local stratification, the thermal structure of nonlinear internal waves and their speed were inferred using the DJL model. The results were consistent with simultaneous and collocated thermistor data acquired in the South China Sea experiments, although the model comparison is limited by the assumptions of an isolated steady state and the neglect of rotation effects.

Although the present discussion was motivated by our interest in using the pressure-equipped inverted echo sounder to study nonlinear internal waves, the techniques developed, including estimation of travel time and evaluation of bias as a function of sea state, will have application to measurements taken in other environments and for other purposes.

Acknowledgments. We gratefully acknowledge the assistance of many individuals in this project. We thank Erran Sousa for his help in deployment and recovery of the instruments; Gerard Chaplin for modifications to the instrument setup; Randolph Watts, Jae-Hun Park, and Mark Wimbush for many helpful discussions; and an anonymous referee for comments. A version of the Turkington code was kindly made available to us by Dr. Frank Henyey, University of Washington. Georges Dossot and James Miller provided valuable computing support, and the crews of the R/V *Melville* and R/V *OR1* assisted us with operations at sea. We are especially grateful to David Tang of the Institute of Oceanography, National Taiwan University, for making the *OR1* available to us. This project was supported by the ONR Nonlinear Wave Program under Contract N0014-05-1-0286.

REFERENCES

Apel, J. R., L. A. Ostrovsky, Y. A. Stepanyants, and J. F. Lynch, 2007: Internal solitons in the ocean and their effect on underwater sound. *J. Acoust. Soc. Amer.,* **121,** 695–722.

Baines, P. G., 1995: *Topographic Effects in Stratified Flows*. *Cambridge Monogr. Mech.,* Cambridge University Press, 500 pp.

Beckmann, P., and A. Spizzichino, 1963: *The Scattering of Electromagnetic Waves from Rough Surfaces*. Macmillan, 503 pp.

Brown, M. V., and J. Ricard, 1960: Fluctuations in surface reflected pulsed CW arrivals. *J. Acoust. Soc. Amer.,* **32,** 1551–1554.

Charnock, H., 1955: Wind stress on a water surface. *Quart. J. Roy. Meteor. Soc.,* **81,** 639–640.

Clay, C. S., 1960: Fluctuations of sound reflected from the sea surface. *J. Acoust. Soc. Amer.,* **32,** 1547–1551.

Dubriel-Jacotin, M. L., 1932: Sur Les ondes de type permanent dans les liquids heterogens. *Atti. Accad. Lincei Rend. Cl. Sci. Fis. Mat. Nat.,* **6,** 814–819.

Duda, T. F., 2006a: Initial results from a Cartesian three-dimensional parabolic equation acoustical propagation code. Woods Hole Oceanographic Institute Tech. Rep. WHOI-2006-14, 17 pp.

——, 2006b: Temporal and cross-range coherence of sound traveling through shallow-water nonlinear internal wave packets. *J. Acoust. Soc. Amer.,* **119,** 3717–3725.

——, and D. M. Farmer, 1998: WHOI/IOS/ONR Internal Solitary Wave Workshop: Contributed papers. Woods Hole Oceanographic Institute Tech. Rep. WHOI-99-07, 248 pp.

Eckart, C., 1953: The scattering of sound from the sea surface. *J. Acoust. Soc. Amer.,* **25,** 566–570.

Farmer, D. M., and D. D. Lemon, 1984: The influence of bubbles on ambient noise in the ocean at high wind speeds. *J. Phys. Oceanogr.,* **14,** 1762–1778.

——, D. Li, B. Donald, and L. Martin, 2002: Wave kinematics at high sea states. *J. Atmos. Oceanic Technol.,* **19,** 225–239.

Fortuin, L., 1970: Survey of literature on reflection and scattering of sound waves at the sea surface. *J. Acoust. Soc. Amer.,* **47,** 1209–1228.

Helfrich, K. R., and W. K. Melville, 2006: Long nonlinear internal waves. *Annu. Rev. Fluid Mech.,* **38,** 395–425.

Holford, R. L., 1981: Scattering of sound waves at a periodic, pressure-release surface: An exact solution. *J. Acoust. Soc. Amer.,* **70,** 1116–1128.

Jackson, C., 2007: Internal wave detection using the Moderate Resolution Imaging Spectroradiometer (MODIS). *J. Geophys. Res.,* **112,** C11012, doi:10.1029/2007JC004220.

Kitaigorodskii, S. A., 1992: The dissipation subrange of wind-wave spectra. *Proc. Breaking Waves. Symp.,* Sydney, Australia, Int. Union of Theoretical and Applied Mathematics, 200–206.

Knudsen, V. O., R. S. Alford, and J. W. Emling, 1948: Underwater ambient noise. *J. Mar. Res.,* **3,** 410–429.

Kur'ynov, B. F., 1963: The scattering of sound at a rough surface with two. Types of irregularity. *Sov. Phys. Acoust.,* **8,** 252–257.

Long, R. R., 1953: Some aspects of the flow of stratified fluids. I. A theoretical invertigation. *Tellus,* **5,** 42–57.

McDaniel, S. T., 1986: Diffractive corrections to the high-frequency Kirchhoff approximation. *J. Acoust. Soc. Amer.,* **79,** 952–957.

——, 1993: Sea surface reverberation: A review. *J. Acoust. Soc. Amer.,* **94,** 1905–1922.

——, and A. D. Gorman, 1983: An examination of the composite-roughness scattering model. *J. Acoust. Soc. Amer.,* **73,** 1476–1486.

Moum, J. N., and W. D. Smyth, 2006: The pressure disturbance of a nonlinear internal wave train. *J. Fluid Mech.,* **558,** 153–177.

Phillips, O. M., 1985: Statistical and spectral properties of the equilibrium range in the spectrum of wind-generated gravity waves. *J. Fluid Mech.,* **156,** 505–531.

——, F. L. Posner, and J. P. Hansen, 2001: High range resolution radar measurements of the speed distribution of breaking events in wind-generated ocean waves: Surface impulse and wave energy dissipation rates. *J. Phys. Oceanogr.,* **31,** 450–460.

Pierson, W. J., and L. Moskowitz, 1964: A proposed spectrum form for fully developed wind seas based on the similarity theory of S. A. Kitaigorodskii. *J. Geophys. Res.,* **69,** 5181–5191.

Rayleigh, J. W. S., 1877: *The Theory of Sound*. Vol. 1. MacMillan, 326 pp.

Rice, S. O., 1951: Reflection of electromagnetic waves from slightly rough surfaces. *Commun. Pure Appl. Math.,* **4,** 351–378.

Rossby, T., 1969: On monitoring depth variations of the main thermocline acoustically. *J. Geophys. Res.,* **74,** 5542–5546.

Terrill, E., and W. K. Melville, 1997: Sound-speed measurements in the surface-wave layer. *J. Acoust. Soc. Amer.,* **102,** 2607–2625.

Thomson, D. J., and N. R. Chapman, 1983: A wide-angle split-step algorithm for the parabolic equation. *J. Acoust. Soc. Amer.,* **74,** 1848–1854.

Turkington, B., A. Eydeland, and S. Wang, 1991: A computational method for solitary internal waves in a continuously stratified fluid. *Stud. Appl. Math.,* **85,** 93–127.

Urick, R. J., 1983: *Principles of Underwater Sound*. McGraw-Hill, 423 pp.

Watts, D. R., C. Sun, and S. Rintoul, 2001: A two-dimensional gravest empirical mode determined from hydrographic observations in the Subantarctic Front. *J. Phys. Oceanogr.,* **31,** 2186–2209.

Wenz, G. M., 1962: Acoustic ambient noise in the ocean: Spectra and sources. *J. Acoust. Soc. Amer.,* **34,** 1936–1956.